Hindawi
Geofluids
Volume 2022, Article ID 3964502, 15 pages
https://doi.org/10.1155/2022/3964502

Research Article

Design and Optimization of a Triangular Shear Piezoelectric Acceleration Sensor for Microseismic Monitoring

Yannan Shi[1,2] **Shuaishuai Jiang**[1] **Yang Liu**[3] **Yiying Wang**[1] **and Penglei Qi**[1]

[1]*School of Mechanical and Equipment Engineering, Hebei University of Engineering, Handan 056038, China*
[2]*Handan Key Laboratory of Intelligent Vehicle, Handan 056038, China*
[3]*School of Mechanical Electronic & Information Engineering, China University of Mining and Technology (Beijing), Beijing 100083, China*

Correspondence should be addressed to Yang Liu; liuyangebox@126.com

Received 10 December 2021; Revised 23 March 2022; Accepted 28 March 2022; Published 25 April 2022

Academic Editor: Gangwei Fan

Aiming at the characteristics of low sensitivity and narrow frequency range of existing microseismic monitoring sensors for mine water hazard prevention and control, a piezoelectric acceleration sensor for microseismic monitoring based on a kind of triangular shear structure is proposed. Firstly, the structure of the triangular shear piezoelectric acceleration sensor is designed, and its dynamic model is built. The structural and material parameters related to natural frequency and sensitivity are analyzed. Then, the selection of piezoelectric ceramic materials is discussed. The parametric design of the designed sensor is carried out, and its finite element structural model is built by ANSYS. The modal analysis, resonance response analysis, and piezoelectric analysis of the designed sensor are carried out. The simulation results indicate that the working frequency and sensitivity of the designed sensor meet the requirements of microseismic monitoring. Response surface optimization is adopted to analyze the influence of sensor element design variables on the sensitivity and resonant frequency of the designed sensor. The reoptimized design of the reference sensor improves the resonant frequency of the designed sensor by 9.46% and the charge sensitivity by 18.96%. Finally, the designed sensor is calibrated, and the microseismic signal detection experiment is carried out. The results indicate that the resonant frequency of the designed sensor is 6150 Hz, the working frequency is 0.1-2050 Hz, and the charge sensitivity is 1600 pC/g. The sensor can detect microseismic signals with a wide frequency range and high sensitivity.

1. Introduction

In recent years, mine water inrush dynamic disasters caused by mining activities have occurred frequently, which has become one of the main disasters that continue to threaten coal mine safety production. The possibility of water inrush dynamic disasters in mines will further aggravate with the increase of mining depth [1]. It damages mining equipment and facilities, affects safe production, and threatens the lives of miners. Microseismic monitoring technology has been widely used as an effective means to deal with the above disaster [2]. This technology uses sensors to sense the microseismic signals generated by rock fracture during the formation of coal mine water inrush channel, locate the microseismic time, explain the focal mechanism, and realize the real-time, continuous, and full space prediction of mine water inrush events [3]. As an important part of the microseismic monitoring system, the performance of the sensor is essential to the prediction accuracy of mine water inrush events. Therefore, it is an urgent problem to develop a sensor with a wide working frequency and high sensitivity to improve the comprehensiveness and accuracy of microseismic signal acquisition.

The interferometric optical fiber geophone has high sensitivity and wide dynamic range, which is suitable for detecting microseismic signals. In 2004, Tsinghua University developed a three-component mandrel optical fiber accelerometer, which can be used for downhole petroleum exploration [4]. The working frequency band is 3~800 Hz, and the on-axial acceleration sensitivity is 39 dB re rad/g. Optical fiber microseismic detection technology is widely used in petroleum geophysical exploration, but in the fields with poor production conditions

such as coal mines, the performance of the sensor needs to be further improved. The sensitivity of the piezoelectric accelerometer developed in [5] is 19 V/g, and the dynamic range is 80 dB. The piezoelectric six-axis acceleration sensor developed in [6] uses a single inertial mass, which can measure the six-axis acceleration and is linearly coupled in all directions. The axial sensitivity can reach 0.695 V/g, and the natural frequency can reach 25 kHz. A biaxial differential piezoelectric accelerometer with bimorph and independent mass structure is studied [7]. The resonant frequency of the accelerometer optimized by the finite element method is about 7.4 kHz, and the sensitivity of the two axes is 1556 pC/g and 1363 pC/g, respectively. The natural frequency of the piezoelectric MEMS accelerometer designed in [8] is about 29.8 kHz, and the maximum sensitivity is about 0.2 mV/g, which needs further improvement. Although the MEMS sensor studied in [9] can monitor microseismic signals, its frequency range is small and cannot monitor microseismic signals more comprehensively.

The performance of the piezoelectric accelerometer in bending mode is studied in [10], and the sensitivity is associated with the system parameters by using a set of approximate formulas. The cantilever beam structure of bimorph is adopted, and the sensitivity can reach at least 500 pC/g. A piezoelectric thick film acceleration sensor with large bandwidth and temperature compensation is reported in [11]. Its natural frequency is 40 kHz, and its sensitivity is 6 mV/ms^{-2}. A circular piezoelectric accelerometer is developed by using PZT thick film material with a large piezoelectric coupling coefficient in [12, 13]. Its sensitivity can reach 7.6 pC/g, the resonance frequency is about 3.7 kHz, and the structure is more robust. A shear-mode high-temperature piezoelectric acceleration sensor is studied by using YCOB Crystal in [14], which can withstand the high-temperature environment of 1250°C, and the sensitivity value is 8.7 ± 1.6 pC/g. Compared with the PZT accelerometer with a similar structure, the piezoelectric accelerometer adopts BNKBT lead-free ceramic ring as a sensing element, which has good performance and wide frequency response [15]. The platformed unimorph accelerometer adopts a curved plate with a castellated surface to form a sensing structure, which will increase the stress in the piezoelectric crystal and produce higher charge output. The accelerometer has the characteristic that the noise is inversely proportional to the charge output at the low frequency [16]. A sensor using Li-doped ZnO film with a double piezoelectric layer structure is proposed in [17]. This sensor can obtain the maximum output at the resonance frequency. Moreover, the output sensitivity can be improved with the above structure.

The MOEMS accelerometer designed in [18] uses a micromechanical sensing structure and a grating interferometer to exhibit low cross-axis sensitivity. Under the optimum design conditions, the sensitivity of the accelerometer is 2485 V/g, and the resonance frequency is 34.5 Hz. MEMS accelerometers can be designed using various types of piezoelectric materials. By studying the bulk phase and thin-film form of piezoelectric materials, high-performance MEMS accelerometers can be configured using microprecision machining or hybrid integration methods [19, 20]. The piezoelectric geophone with a multilayer spiral corrugated cantilever beam has a low natural frequency due to the long structure of the cantilever beam, and the corrugated structure improves its sensitivity [21, 22].

In addition, numerical simulation can be used to visualize several specifics that cannot be obtained in experiments. Therefore, appropriate analysis models can be used to explain the function of design variables and the relationship between variables and performance [23]. Although the above methods are of strategic significance in the research and development of sensors, when microseismic monitoring is applied in coal mines, the frequency range of sensors needs to reach 1500 Hz and have enough sensitivity.

Based on the above literature collection and analysis, a piezoelectric acceleration sensor for microseismic monitoring based on a kind of triangular shear structure is designed. The structure is improved based on the basic triangular shear structure to improve the sensitivity of the designed sensor. The dynamic model is analyzed, and the material of the sensor is selected. Then, the parametric design of the piezoelectric acceleration sensor is carried out. The finite element model of the designed sensor is built by ANSYS, and its structural rationality, resonant frequency, and sensitivity are analyzed. The sensitivity and resonant frequency are optimized by the response surface optimization method. Finally, the prototype of the designed sensor is developed, and its design scheme, theoretical calculation, and simulation analysis are verified by experiments.

2. Scheme Design and Working Principle

2.1. Structure Design. The structure of the piezoelectric acceleration sensor mainly includes the compression type, shear type, and bending type. Among them, the compression acceleration sensor has the merits of high mechanical strength and resonance frequency. The bending type has low mechanical strength and resonance frequency, but high sensitivity. The shear structure has the characteristics of small volume, high mechanical strength, high resonance frequency, resistance to substrate deformation, and temperature impact and can measure low-frequency signals [24]. Microseism is a small vibration caused by rock fracture or fluid disturbance. To detect microseismic signals more accurately and comprehensively, it is necessary to ensure that the sensor has a high resonance frequency and sufficient sensitivity. Therefore, the triangular shear structure is selected in the design of the sensor. Figure 1 shows the structure of the triangular shear piezoelectric acceleration sensor, which consists of the piezoelectric element, base, shell, conductive sheet, insulating sheet, seismic mass, and fastener. Moreover, in order to intuitively obtain the information of different components of the sensor, the 3D view inside the shell is shown in Figure 2. The piezoelectric elements are distributed on the three planes of the regular triangular prism of the base. The piezoelectric elements, the conductive sheet, and the seismic mass are fixedly connected to the base through the radial force generated by the extrusion of the insulating sheet by the fastener. Compared with other types of piezoelectric acceleration sensors, separating the piezoelectric

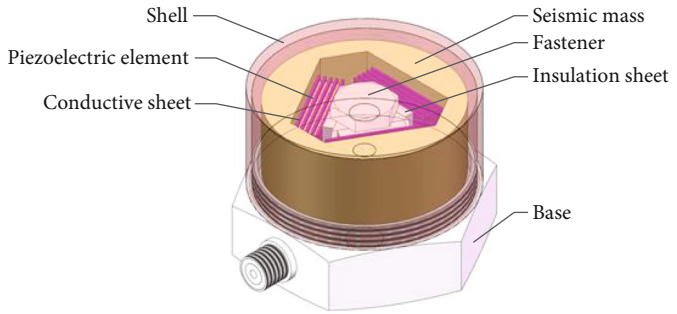

Figure 1: Structure of the triangular shear piezoelectric acceleration sensor.

element from the base can reduce the effects of thermal transient and base bending [14].

The active component of the sensor in Figure 2 is the piezoelectric element. When the sensor receives a microseismic signal, the shear force is equal to the product of the acceleration received by the seismic mass and the mass acting on each piezoelectric element. The piezoelectric element generates an electric charge proportional to the shear force. There are four independent piezoelectric elements on each side, and the connection form is electrical parallel output. The triangular shear structure has three sides, and each side is also the electrical parallel output. The output voltage is the voltage of a single piezoelectric element, and the amount of charge is the sum of all piezoelectric elements.

2.2. Working Principle. The working principle of the piezoelectric acceleration sensor is to convert the acceleration signal to be measured into an electrical signal based on the positive piezoelectric effect of the piezoelectric crystal. The dynamic model of the sensor can be equivalent to a single degree of freedom system, including mass (m)-spring (k)-damping (c) [25, 26], as shown in Figure 3. The sensor base is connected to the vibrating surface. When the sensor senses the acceleration signal, the piezoelectric element deforms under the action of the inertia force of the mass, causing the change of charge and realizing the conversion from the acceleration signal to the electrical signal.

In Figure 3, the mass of the seismic mass in the shell of the sensor is m. The piezoelectric material and friction resistance in the sensor are expressed by spring and damper, respectively, and the stiffness coefficient and damping coefficient are k and c, respectively. When an external vibration signal is sensed by the sensor, a displacement response $x_i(t)$ will be generated on the vibrating surface. Under the action of inertia, the vibration displacement of the seismic mass is $x_m(t)$, and its displacement $x_o(t)$ relative to the base can be expressed as

$$x_o(t) = x_m(t) - x_i(t). \tag{1}$$

Under the action of the spring and damper, the motion equation of the seismic mass can be expressed as

$$m\frac{d^2x_m(t)}{dt^2} = -kx_o(t) - c\frac{dx_o(t)}{dt}. \tag{2}$$

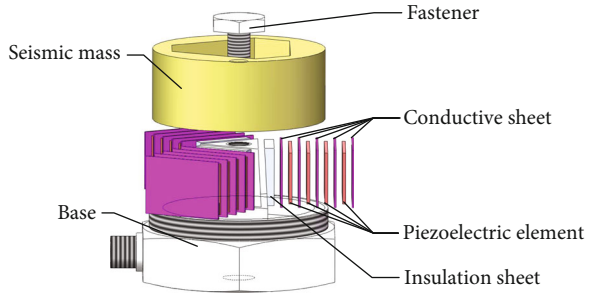

Figure 2: 3D view inside the shell of the sensor.

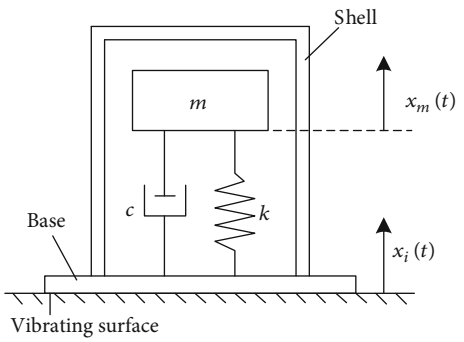

Figure 3: Dynamic model of the piezoelectric acceleration sensor.

Substituting equation (1) in equation (2), the differential equation of the system can be obtained as

$$m\frac{d^2x_o(t)}{dt^2} + c\frac{dx_o(t)}{dt} + kx_o(t) = -m\frac{d^2x_i(t)}{dt^2} = -ma, \tag{3}$$

where a is the measured acceleration.

The Fourier transform of equation (3) is obtained as

$$\frac{x_0(j\omega)}{a} = -\frac{(1/\omega_n)^2}{1-(\omega/\omega_n)^2 + 2\zeta(\omega/\omega_n)j}, \tag{4}$$

where ω_n and ζ can be evaluated as the following:

$$\omega_n = \sqrt{\frac{k}{m}}, \tag{5}$$

Table 1: The specific nonpiezoelectric materials and their properties of the designed sensor.

Component	Material	Young's modulus (N/m^2)	Density (kg/m^3)	Poisson's ratio
Seismic mass	Tungsten alloy	34×10^{10}	17500	0.27
Base	Stainless steel	20×10^{10}	7860	0.3
Conductive sheet	Brass	10.4×10^{10}	8600	0.37
Insulation sheet	Alumina ceramic	30×10^{10}	3600	0.24
Shrink ring	Aluminium alloy	9×10^{10}	2700	0.32

Table 2: The electrical and mechanical properties of the piezoelectric material.

Material	Density (kg/m^3)	Piezoelectric constant (pC/N)			Poisson's ratio	Modulus of elasticity (GPa)					
		d_{31}	d_{33}	d_{15}		C_{11}^E	C_{12}^E	C_{13}^E	C_{33}^E	C_{44}^E	C_{66}^E
PZT-5H	7800	-274	593	741	0.33	126	79.5	84.1	117	23	23.5

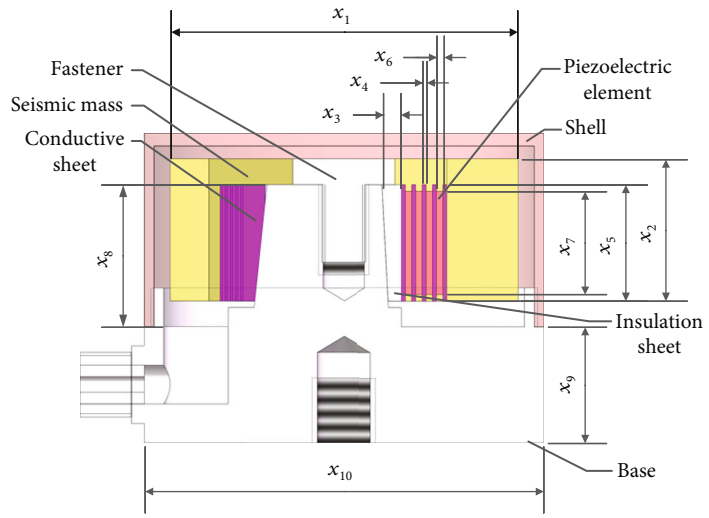

Figure 4: Ten design variables of numerical analysis.

$$\xi = \frac{c}{2\sqrt{km}}, \tag{6}$$

where ω_n and ζ are the natural frequency and damping ratio of the sensor, respectively.

From equation (4), it can be concluded that the natural frequency is one of the important parameters affecting the dynamic characteristics of the sensor, which is determined by the equivalent mass and stiffness constant. The resonant frequency of the sensor can be given by

$$f_n = \frac{1}{2\pi}\sqrt{\frac{k}{m}}. \tag{7}$$

Therefore, the following relationship can be obtained from equation (4):

$$\left|\frac{x_0}{a}\right| = \frac{1}{\omega_n^2\sqrt{\left[1-(\omega/\omega_n)^2\right]^2 + (2\zeta\omega/\omega_n)^2}}. \tag{8}$$

In a specific frequency range, the inertial force exerted by the seismic mass on the piezoelectric element is alternating stress exerted, and the seismic mass approximately obeys Newton's second law:

$$F = ma, \tag{9}$$

where F is the inertial force.

Table 3: Ten design variables and their size ranges.

Design variable	Description	Reference size (mm)	Size range (mm)
x_1	Seismic mass diameter	27	26–28
x_2	Seismic mass height	11	10–12
x_3	Insulation sheet thickness	1.5	1.4–1.6
x_4	Conductive sheet thickness	0.3	0.25–0.35
x_5	Conductive sheet height	9	8–9
x_6	Piezoelement thickness	0.5	0.4–0.6
x_7	Piezoelement height	8	7–8
x_8	Base triangular prism height	11	10–12
x_9	Base thickness	9	7–9
x_{10}	Base inscribed circle outer diameter	31	30–32

Under the fixed premise, the amount of charge Q generated on the piezoelectric element is directly proportional to the force F:

$$Q = d_{ij}F = d_{ij}ma = d_{ij}kx_o(t), \tag{10}$$

where d_{ij} is the piezoelectric constant of the piezoelectric element.

Combining equations (8) and (10), the charge sensitivity of the sensor is obtained by

$$S_Q = \left|\frac{Q}{a}\right| = \frac{d_{ij}k}{\omega_n^2\sqrt{\left[1-(\omega/\omega_n)^2\right]^2 + (2\zeta\omega/\omega_n)^2}}, \tag{11}$$

where S_Q is the charge sensitivity.

Therefore, the sensitivity of the sensor is inversely proportional to the natural frequency and directly proportional to the piezoelectric coefficient. The designed sensor will compromise between high resonant frequency and high sensitivity [27]. When designing the sensor, the sensitivity can be improved by selecting materials with a high piezoelectric coefficient or reducing the natural frequency.

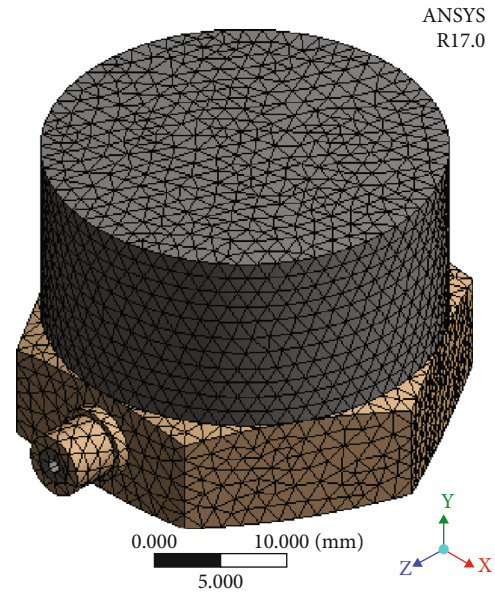

Figure 5: Finite element model of the designed sensor.

2.3. Material Selection. The designed sensor in this paper adopts a triangular shear structure, and the piezoelectric constant of the piezoelectric effect is mainly d_{15}. Commonly used piezoelectric materials mainly include SiO_2, $BaTiO_3$, PZT, and PVDF. Through the comparison of material properties, it is concluded that PZT-5H has a greater piezoelectric constant than other types of piezoelectric materials. In addition, the material has high dielectric properties and electromechanical coupling coefficient, which makes it have high sensitivity and fast response. More importantly, the temperature and time stability of the electromechanical parameters are strong. Because PZT-5H has better piezoelectric performance, the piezoelectric element of the sensor designed in this paper adopts PZT-5H.

According to the relevant data, the material selection of each sensor component is determined. The specific nonpiezoelectric materials and their properties are shown in Table 1. The electrical and mechanical properties of the piezoelectric material are shown in Table 2.

2.4. Parameterization Design. Design of Experiments (DOE) [28] has been used for effective simulation experiments. Using DOE test points, the resonant frequency and voltage are numerically calculated through modal analysis and piezoelectric analysis. The numerical modeling method approximately uses DOE test points to solve the relationship between design variables and performance.

Taking the YD-62 piezoelectric acceleration sensor as a reference sensor, the geometric standard of the internal components of the sensor is deduced. Ten design variables determined by the reference sensor are shown in Figure 4, and their size ranges are shown in Table 3.

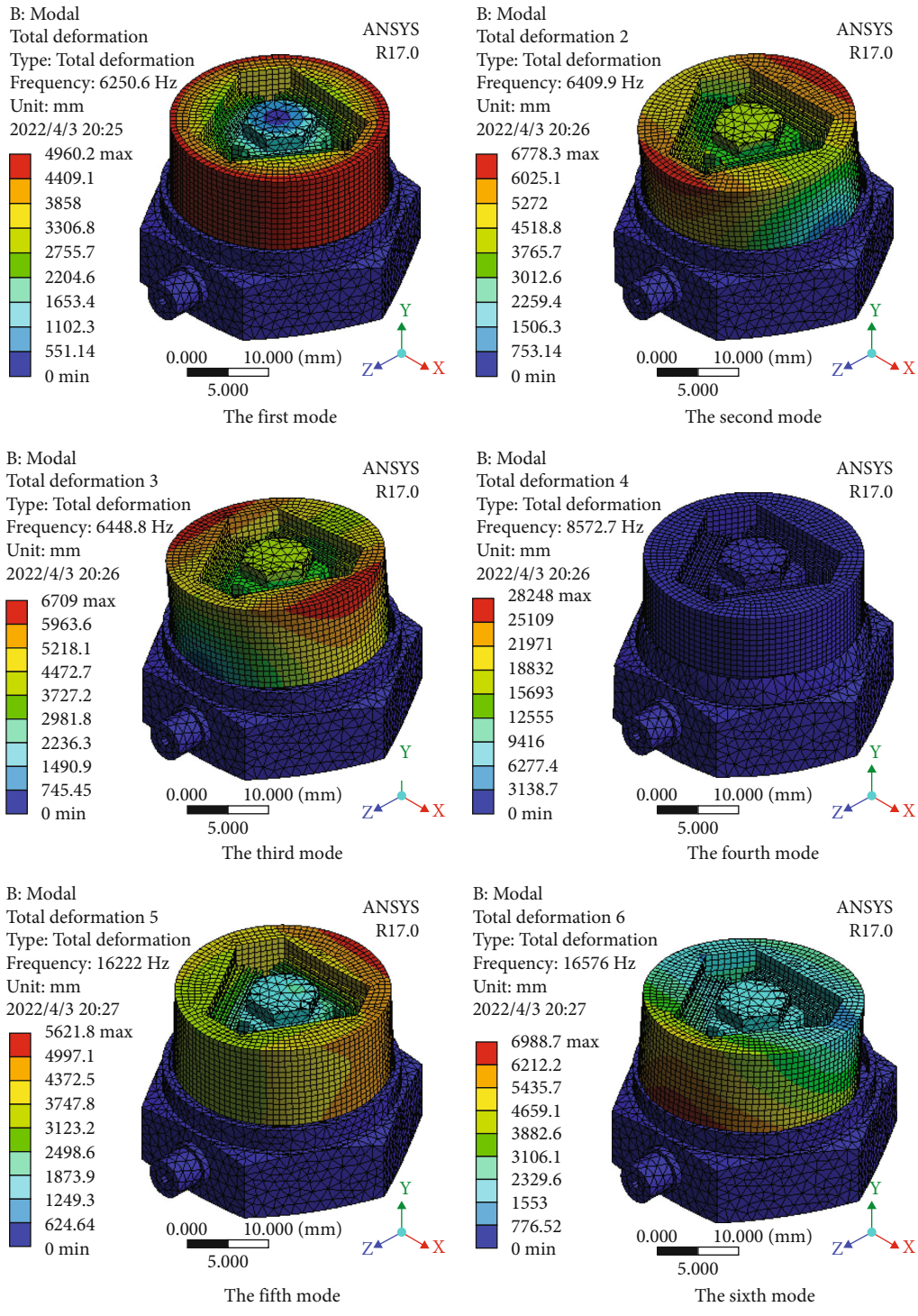

Figure 6: The first to sixth vibration modes.

3. Finite Element Analysis

According to the geometric and material parameters of the piezoelectric acceleration sensor, the structural model of the designed sensor is built by SOLIDWORKS, and the contact constraints are set in the assembly. Then, the above structural model is imported into ANSYS to build the finite element model of the designed sensor. At the same time, the original contact constraint is automatically transformed into bonded constraint. Then, the material parameters such as piezoelectric matrix, stiffness matrix, and dielectric constant are input. When meshing, the piezoelectric material part of the sensor is selected as SOLID226 element, and the metal material part is selected as SOLID186 element. The base and shell are meshed by tetrahedral elements, and other elements are hexahedral elements. The polarization direction of

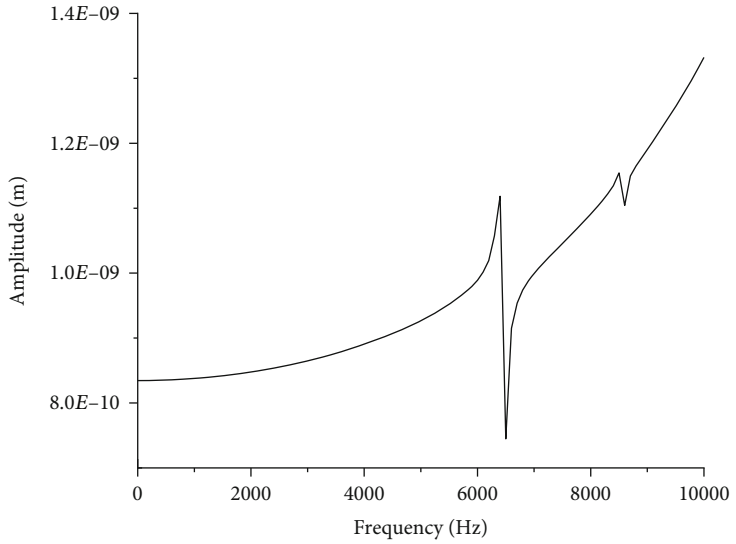

Figure 7: Sensor resonance frequency response.

each piezoelectric element is set by defining the local coordinate system, and then, the corresponding electrode surface is added. The fixed displacement constraint is added to the bottom surface of the sensor, and the acceleration load is applied to the whole model [29]. Figure 5 shows the meshing result of the sensor finite element model. The total number of elements and nodes is 42990 and 127838, respectively. Through modal analysis, harmonic response analysis, and piezoelectric analysis, the sensitivity and resonance frequency of the sensor can be calculated.

3.1. Modal Analysis. An important characteristic of the piezoelectric acceleration sensor is the response to different resonance frequencies, which can be studied by modal analysis. The upper cut-off frequency of the sensor depends on the resonance frequency of the amplitude-frequency curve. Dynamic characteristics mainly study the resonance frequency of the structure under dynamic load, which is an important parameter in structural design. The resonance frequency can be determined by modal analysis of the designed sensor using ANSYS [30]. Figure 6 shows the vibration modes of the designed sensor from 1st to 6th.

It can be concluded from the simulation results that the vibration frequencies from the first to the sixth mode are 6250.6 Hz, 6409.9 Hz, 6448.8 Hz, 8572.7 Hz, 16222 Hz, and 16576 Hz, respectively. There is a certain gap between the first and second modes of the sensor. The second mode is very close to the third mode, and they gradually increase rapidly from the third mode. The first mode is the rotational movement of the parts in contact with the triangular prism around the Y-axis. The main position of the second and third deformation modes is the bottom area of the triangular prism of the base, but the direction of bending deformation is orthogonal. The main position of the fourth mode deformation is the upper surface of the shell, and the fifth and sixth mode deformations are mainly caused by the deformation and sliding of piezoelectric elements and conductive

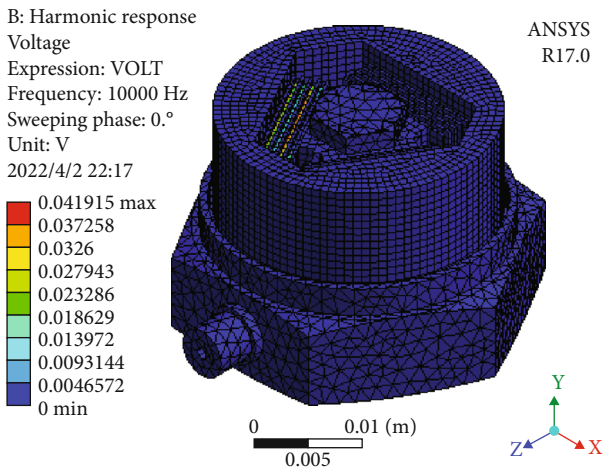

Figure 8: Voltage distribution diagram of the designed sensor.

sheets caused by the seismic mass. From the above analysis, the resonant frequency of the sensor is 6250.6 Hz. According to the amplitude-frequency characteristics of the sensor, 1/3 of the resonant frequency is taken as the upper frequency to reduce the amplitude error.

3.2. Harmonic Vibration Response Analysis. The target vibration direction of the sensor is the Y-axis direction. In this paper, the steady-state forced vibration of the sensor is solved by the harmonic response analysis method, and the inertial acceleration load of the microseismic signal is added to the bottom of the base. According to the resonance frequency obtained from modal analysis, the frequency range is tentatively determined as 0-10 kHz. One hundred frequency bands are defined within 0-10 kHz; that is, every 100 Hz is a frequency band [31].

In the equivalent system of the piezoelectric acceleration sensor, the damping coefficient is usually between 0.002 and 0.25. When the damping is air, the damping coefficient is

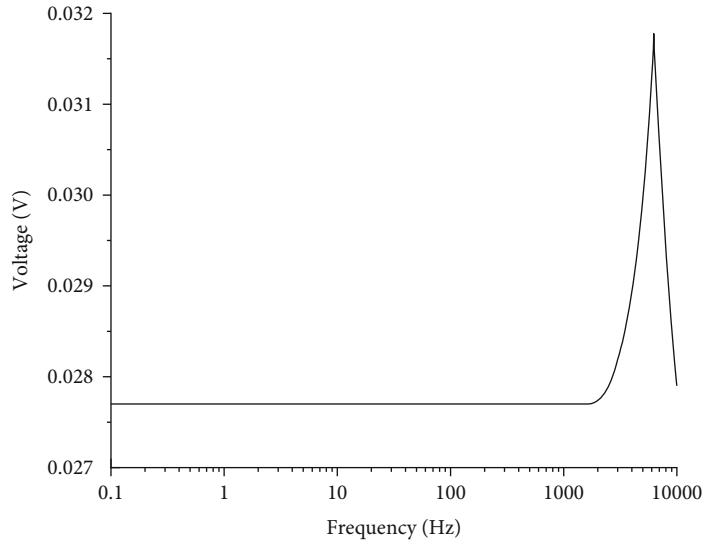

Figure 9: Voltage frequency diagram of the piezoelectric element.

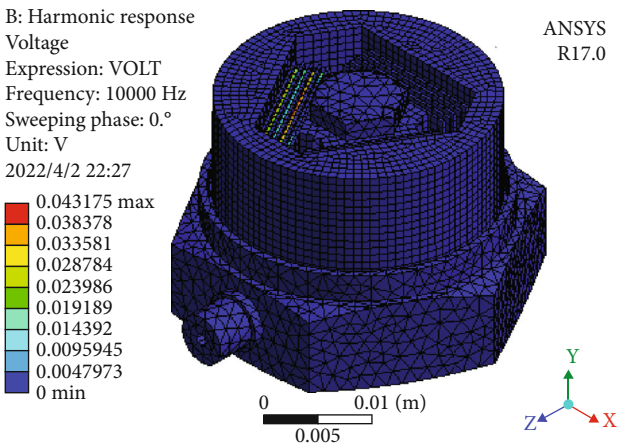

Figure 10: Voltage distribution diagram for case 1.

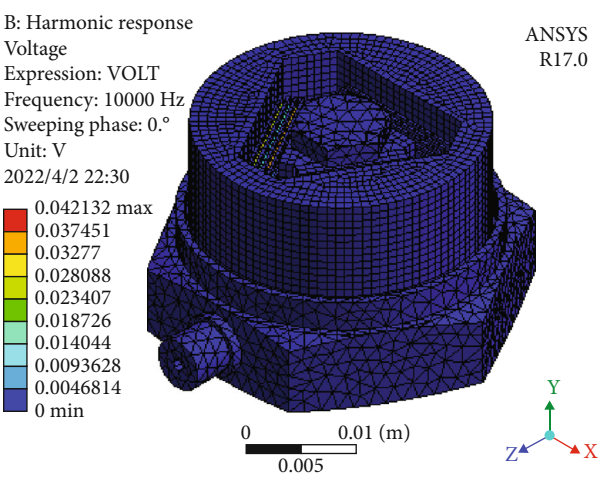

Figure 12: Voltage distribution for case 3.

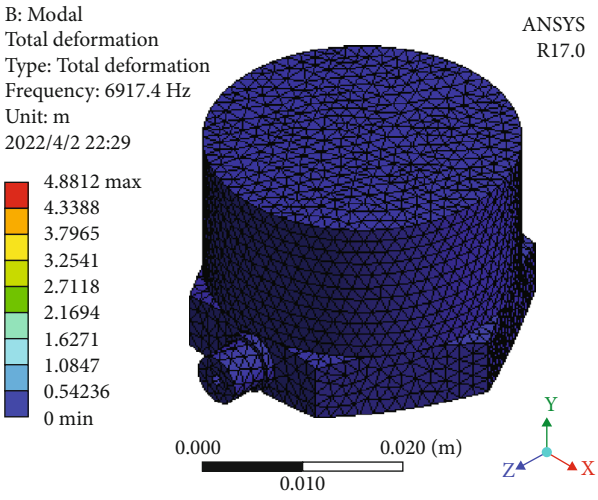

Figure 11: Modal analysis result for case 2.

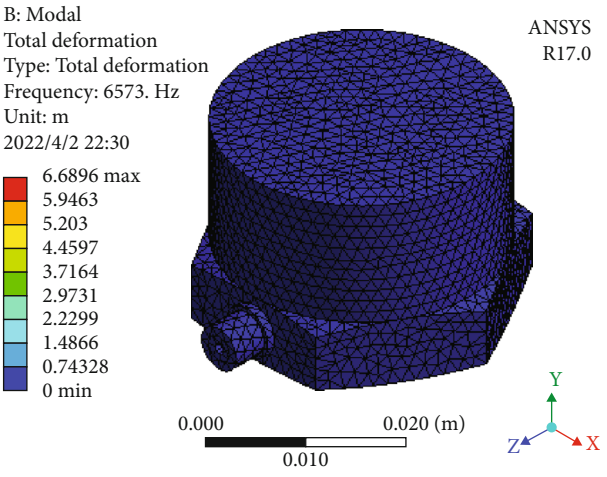

Figure 13: Modal analysis result for case 3.

Table 4: Values of optimized design variables and the results of cases 1, 2, and 3.

Case	x_1 (mm)	x_2 (mm)	x_3 (mm)	x_4 (mm)	x_5 (mm)	x_6 (mm)	x_7 (mm)	x_8 (mm)	x_9 (mm)	x_{10} (mm)	R.F. (Hz)	C.S. (pC/g)
1	27	12	1.4	0.285	8	0.4	7	11	7	30.6	6250	1945
2	26	11.96	1.5	0.3	8	0.4	7	11	7	30	6841.9	1635
3	27	11.17	1.4	0.28	8	0.4	7	10.5	7.8	31	6471.6	1817
Reference	27	11	1.5	0.3	9	0.5	8	11	9	31	6250.6	1635

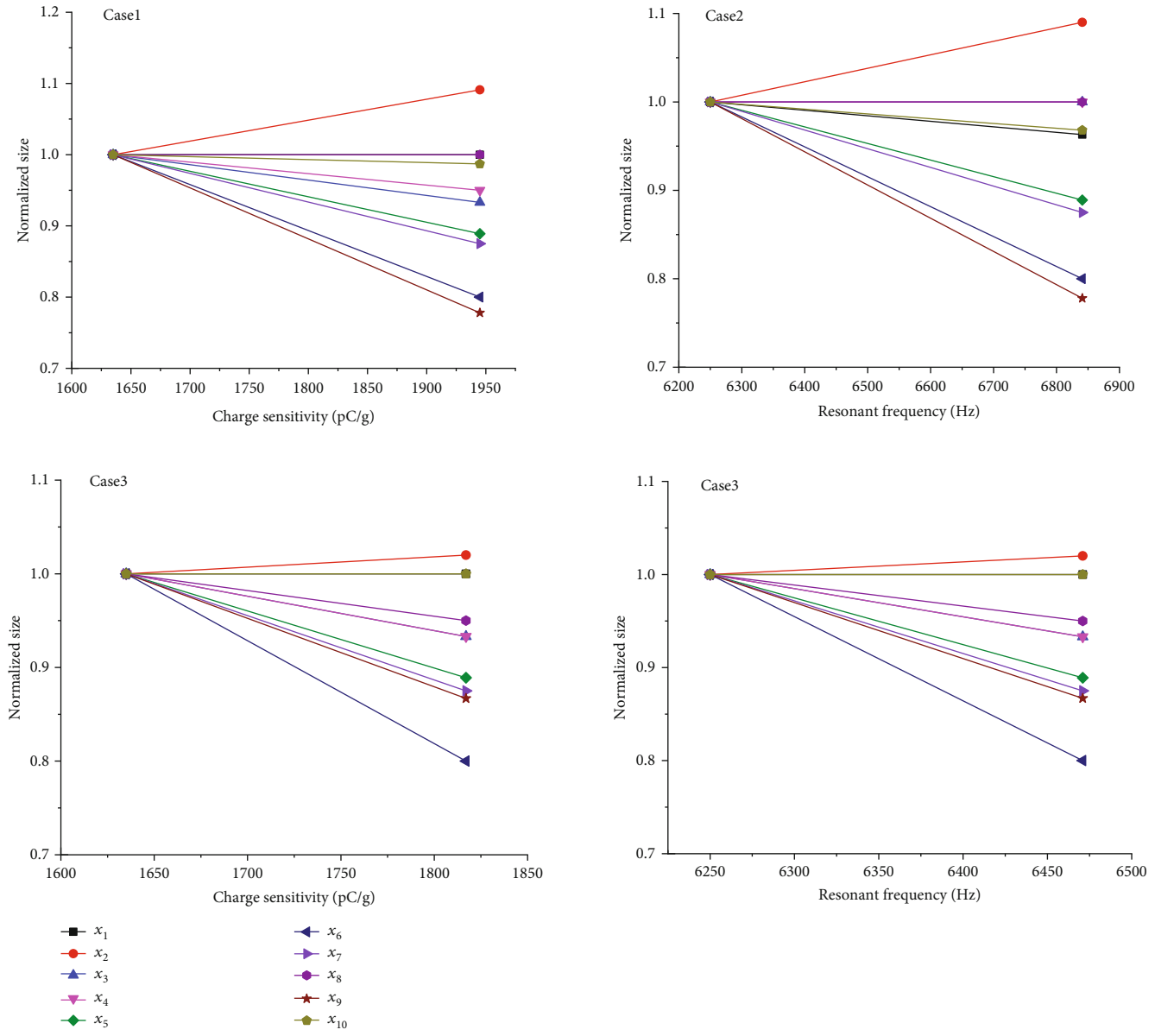

Figure 14: In all cases, the change in the normalized size of each design variable is relative to the reference design.

0.01. Therefore, in the above analysis, the value of the damping coefficient in the equivalent system remains constant ($c = 0.01$) [10]. Under the action of the simulated microseismic acceleration signal, the sensor produces resonant motion. After solving and processing, the harmonic response result of the sensor structure is obtained as shown in Figure 7.

According to the modal analysis results, the resonant frequency of the sensor is 6250.6 Hz. Therefore, the resonance frequency response curve should theoretically reach the peak amplitude at 6250.6 Hz. It can be seen from Figure 7 that the average amplitude of the first half is 8.4×10^{-10} m; the maximum amplitude is 1.1×10^{-9} m, appearing near 6250 Hz. Therefore, the maximum amplitude appears at the resonance

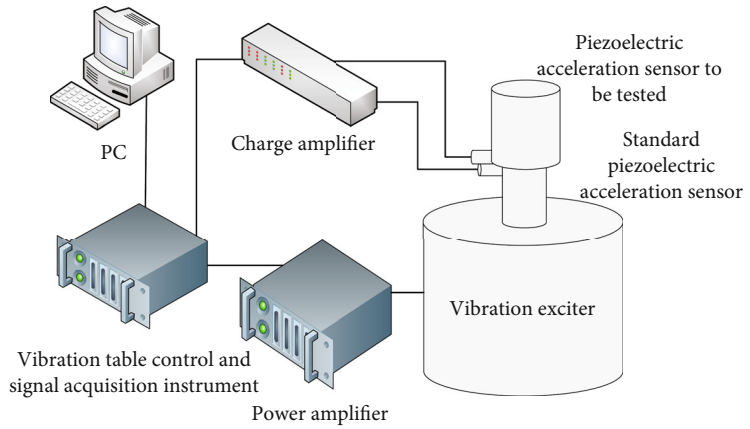

Figure 15: Schematic diagram of sensor calibration experiment test device.

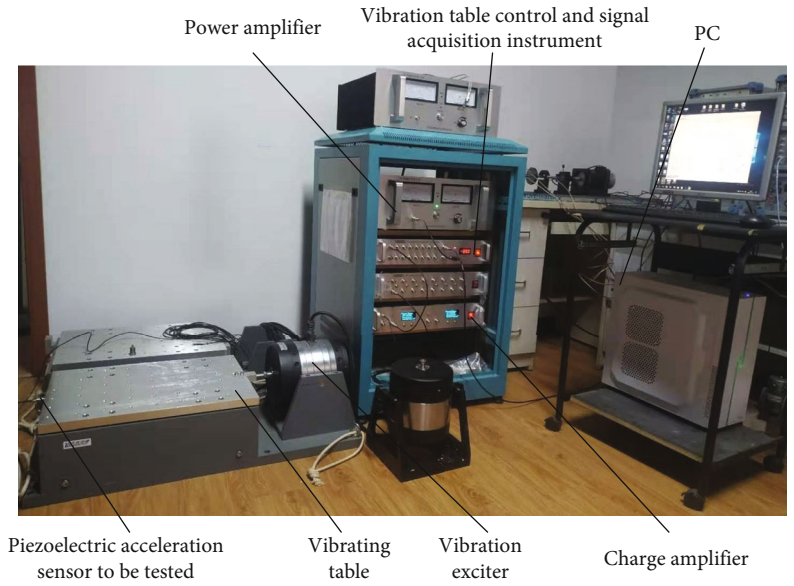

Figure 16: Physical diagram of sensor experimental test device.

frequency of 6250.6 Hz under the acceleration load of the sensor, and the stable working frequency of the sensor is 0-2083 Hz. In this frequency range, the frequency response curve of the sensor is approximately a straight line, which can be stably monitored by microseismic signals. According to Reference [32], the working frequency range of the sensor is 0 to 1/3 of the resonance frequency range. The simulation results verify the correctness of the above conclusion.

3.3. Piezoelectric Analysis. The charge sensitivity of the sensor is simulated based on the harmonic response analysis. Only the open-loop condition of the piezoelectric element is considered in the simulation calculation; that is, only the open-loop output potential of the piezoelectric element under acceleration load is calculated. The two surfaces of the piezoelectric element are set as zero potential constraint and voltage coupling constraint, respectively. Under the action of the external load, the voltage difference between two planes of the piezoelectric element is an amount to be determined [33]. The result of the piezoelectric analysis is shown in Figure 8.

Under the action of the acceleration load, the output voltage frequency diagram of the piezoelectric element is shown in Figure 9. The output voltage of the sensor is linear and stable in the range of 0-2083 Hz, and its charge sensitivity is 1635 pC/g.

3.4. Response Surface Optimization. Since the designed sensor contains many nonlinear features and geometric design variables, the Kriging model is used in response surface analysis, and the global approximation model is used in the metamodel [34]. Using the Kriging model, ten design variables are optimized through the response surface optimization method to determine which design variables will affect the performance of the designed sensor and how much its performance is improved compared to the reference sensor [35]. Therefore, three different cases are used to optimize the performance of the designed sensor, of which

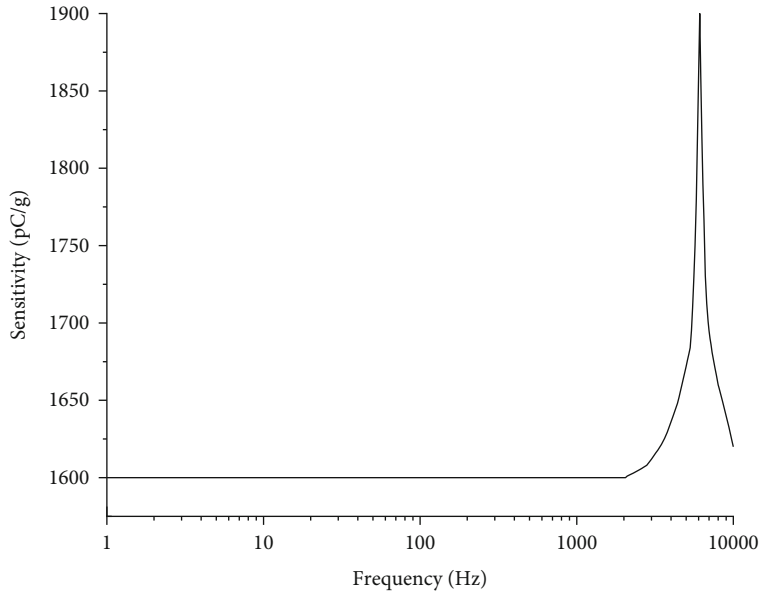

Figure 17: Charge sensitivity frequency response curve.

case 1 is to optimize the charge sensitivity at a constant resonant frequency (6250 Hz). The optimized voltage distribution is shown in Figure 10. Case 2 is to optimize the resonant frequency at a constant charge sensitivity (1635 pC/g). The optimized modal analysis result is shown in Figure 11. Finally, case 3 is used to optimize these two performances. The optimized voltage distribution and modal analysis results are shown in Figures 12 and 13. The optimized numerical analysis results in these three cases are shown in Table 4. Clearly, this optimization has successfully improved one performance (cases 1 and 2) or two performances (case 3).

As can be seen from Table 4, for case 1, the charge sensitivity increased by 18.96% (1945 pC/g), and for case 2, the resonant frequency increased by 9.46% (6841.9 Hz). For case 3, the charge sensitivity increased by 11.13% (1817 pC/g), and the resonance frequency increased by 3.54% (6471.6 Hz).

To study the influence of design variables on target performance in detail, Figure 14 shows the changes of ten design variables in three cases, and their sizes are standardized relative to the reference sensor. For case 1, the design variables that mainly affect the increase of charge sensitivity are $x_2, x_3, x_4, x_5, x_6, x_7, x_9$, and x_{10}. The height of the seismic mass increased by 9.1%; the thickness of the insulation sheet and the height of the conductive sheet decreased by 6.7% and 11.1%, respectively; the thickness and height of the piezoelectric element decreased by 20% and 12.5%, respectively; and the thickness of the base decreased by 22.2%. The influence of other design variables is not obvious (less than 5%). For case 2, the increased resonance frequency is mainly composed of $x_1, x_2, x_5, x_6, x_7, x_9$, and x_{10}. For example, the outer diameter of the seismic mass and the base decreased by 3.7% and 3.2%, respectively, while the height of the seismic mass increased by 8.7%. The remaining changed parameters are the same as in case 1. For case 3, the reason that the performance of both can be increased is that x_1 is increased by 1.5%, x_3 and x_4 are reduced by 6.7%, x_5 is reduced by 11.1%, x_6 is reduced by 20%, x_7 is reduced by 12.5%, x_8 is reduced by 4.5%, and x_9 is reduced by 13.3%.

As a result, the reduction in the thickness of the base and the reduction in the thickness and height of the piezoelectric element have a positive impact on both properties. Since the data of other design variables (seismic mass height and insulation sheet thickness) in Figure 14 show a positive impact on one performance and a negative impact on the other, these variables need to be controlled appropriately by selecting additions or decreases to meet the performance requirements. It is worth noting that the size of the seismic mass is the most obvious factor affecting performance, and the effect is just the opposite. This is proof of the conflict between resonant frequency and seismic mass sensitivity. The above analysis indicates that it is very significant to determine the optimal size of the seismic mass.

4. Results and Discussion

To test the performance of the designed sensor, a sensor experimental test device is built. According to international standards, when calibrating the piezoelectric acceleration sensor, it is necessary to adopt the vibration exciter to provide controllable excitation and record the output signal [36]. The setting of the piezoelectric acceleration sensor calibration experimental test device is shown in Figure 15. WS-5932/U160216-DA2 type vibration table control and signal acquisition instrument are adopted to generate a sinusoidal signal, which is amplified by the GF-500 type 500 W power amplifier and then exerted on the JZ-50 type vibration exciter to produce the required vibration. The WS-4601Z charge amplifier is adopted to amplify the electrical signals

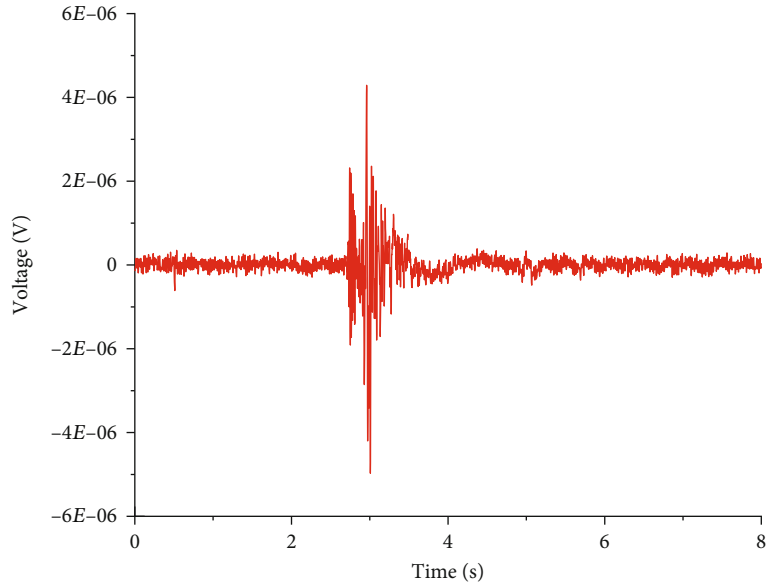

(a) The microseismic signal 1

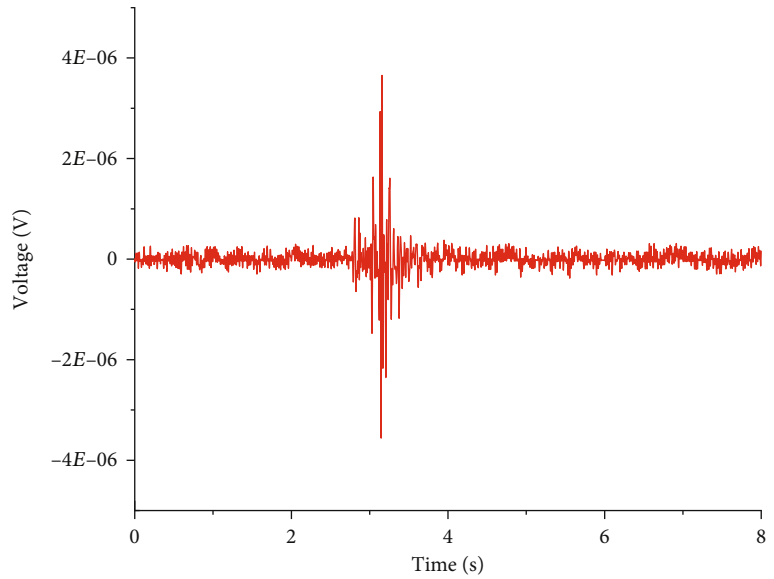

(b) The microseismic signal 2

Figure 18: Continued.

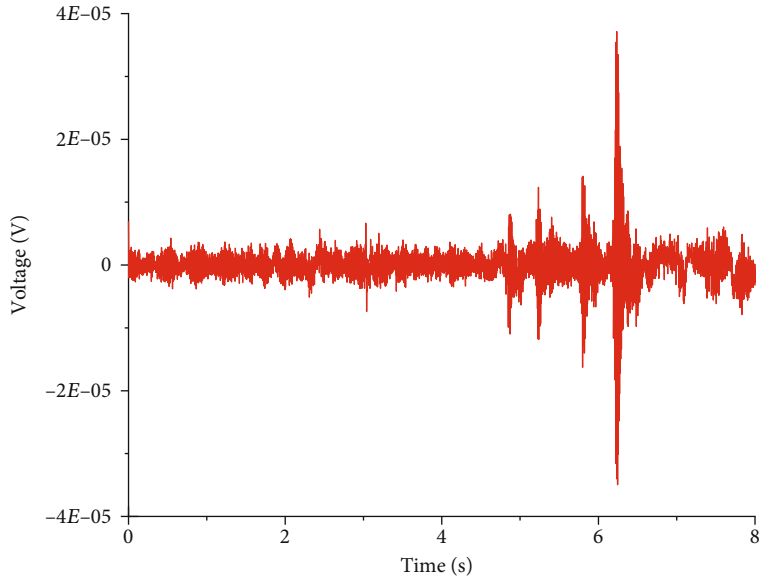

(c) The microseismic signal 3

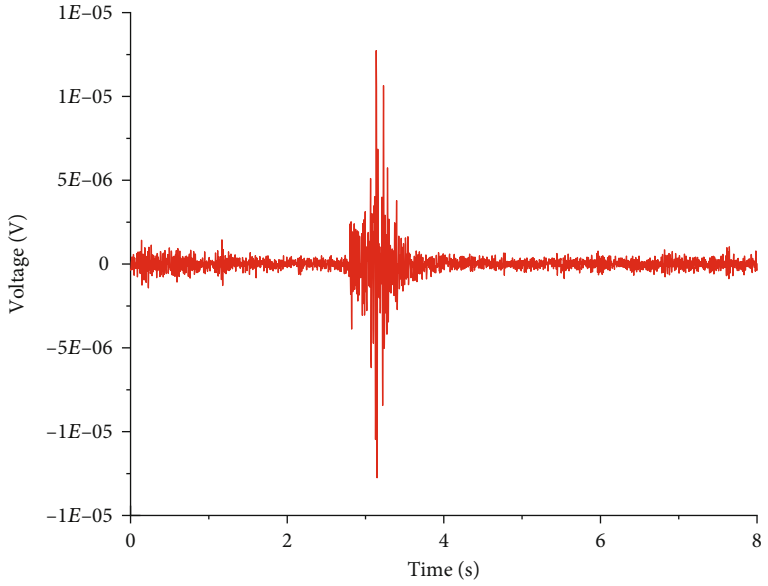

(d) The microseismic signal 4

Figure 18: Waveform of microseismic signals detected by the designed sensor.

from the standard piezoelectric acceleration sensor. The vibration signals detected by the designed sensor are converted into electrical signals through the piezoelectric elements and transmitted to the WS-2411Z charge amplifier. After signal conditioning, they are transmitted to the vibration table control and signal acquisition instrument. After A/D conversion, they are transmitted to a PC for data processing, and the sensitivity test curves of the piezoelectric acceleration sensor and the standard piezoelectric acceleration sensor are recorded.

The standard piezoelectric acceleration sensor is used to measure the acceleration of the vibration exciter. Its model is BK-8305, the charge sensitivity is 1.25 pC/g, and the working frequency is 1-10000 Hz. The back-to-back calibration method is used to measure the sensitivity of the tested sensor.

The experimental test device for the microseismic signal of the piezoelectric acceleration sensor is developed based on the calibration experimental device. Compared with the calibration experimental device, a new vibrating table directly connected to the vibration exciter is added, and the sensor is fixed on the vibrating table for the experimental test. The physical diagram is shown in Figure 16.

When testing the designed sensor, the steady-state sinusoidal excitation method is widely used in the world, which is provided by the vibration exciter. During the test, the sinusoidal signal is output by the vibration controller, amplified by the power amplifier, and then drives the vibrator to

make the measured sensor receive the vibration signal [37]. The charge sensitivity of the designed sensor is calibrated under an excitation signal of 1-10000 Hz. The calibration data is recorded by a computer, and the results are shown in Figure 17.

It can be seen from Figure 17 that the charge sensitivity of the designed sensor is 1600 pC/g, and the resonant frequency is 6150 Hz, so its effective working frequency is 0.1-2050 Hz. There are some errors between the experimental results and theoretical calculation or the finite element simulation. The main reason is that the simulation is set under the ideal conditions of the software without considering processing and assembly errors. In addition, in order to improve the sensitivity of the designed sensor, a more complex structure is adopted, and a certain working frequency range is sacrificed. The complex sensor structure will increase the difficulty of the processing and assembly of the sensor, resulting in large errors between the experimental results and the theoretical analysis or the simulation.

To verify the feasibility of the designed sensor to detect the microseismic signals, the vibration experiments are carried out on the platform shown in Figure 16. Four microseismic signals are selected for experimental verification. The vibration table is driven to vibrate by sending a microseismic signal to the vibration exciter. Then, the designed sensor is used for detection, and the results are shown in Figure 18. The results show that the designed sensor is feasible to detect microseismic signals and has the characteristics of a wide frequency range and high sensitivity.

5. Conclusions

In this paper, a piezoelectric acceleration sensor for microseismic monitoring based on a kind of triangular shear structure is designed and optimized. The piezoelectric element materials and other element materials of the sensor are determined. The modal analysis, resonance response analysis, and piezoelectric analysis of the designed sensor are carried out based on the finite element structural model. The experimental platform is built to verify the feasibility of the sensor to detect microseismic signals. The main conclusions can be drawn as follows:

(1) The natural frequency and sensitivity of the sensor are improved by improving the structure and selecting high-performance materials

(2) The reoptimized design of the reference sensor has successfully improved the performance, the resonant frequency is increased by 9.56%, and the charge sensitivity is increased by 18.96%

(3) The working frequency of the sensor is 0.1-2050 Hz, and the sensitivity is 1600 pC/g, which meets the frequency range and high sensitivity requirements of microseismic signal detection

Clearly, there is a lot of work to do in the future, including analysis of the background noise of the designed sensor, consideration of engineering application and verification in microseismic monitoring system, and further improvement of the working frequency and sensitivity of the piezoelectric acceleration sensor.

Data Availability

The data used to support the findings of this study are available from the corresponding author upon request.

Conflicts of Interest

We all declare that we have no conflict of interest in this paper.

Acknowledgments

This research was supported by the Key R & D Projects of Hebei Province under Grant 19275507D, Hebei Natural Science Foundation Project under Grant E2020402064, and Hebei Innovation Capability Improvement Plan Project under Grant 215676140H.

References

[1] Y. Jiang, Y. Pan, F. Jiang, L. Dou, and Y. Ju, "State of the art review on mechanism and prevention of coal bumps in China," *Journal of China Coal Society*, vol. 39, no. 2, pp. 205–213, 2014.

[2] L. Yuan, Y. D. Jiang, X. Q. He et al., "Research progress of precise risk accurate identification and monitoring early warning on typical dynamic disasters in coal mine," *Journal of China Coal Society*, vol. 43, no. 2, pp. 306–318, 2018.

[3] C. Peng, Y. Chen, Q. Chen et al., "A new type of tri-axial accelerometers with high dynamic range MEMS for earthquake early warning," *Computers & Geosciences*, vol. 100, pp. 179–187, 2017.

[4] N. Zeng, C. Z. Shi, M. Zhang, L. W. Wang, Y. B. Liao, and S. R. Lai, "A 3-component fiber-optic accelerometer for well logging," *Optics Communications*, vol. 234, no. 1-6, pp. 153–162, 2004.

[5] Y. M. Xing, S. H. Liu, and D. X. Wang, "Design and research on piezoelectric acceleration geophone," *Advanced Materials Research*, vol. 468-471, pp. 826–830, 2012.

[6] M. Li, Z. Lin, J. Liu, H. Lv, and L. Qin, "Principle study of a six-axis acceleration sensor," *Chinese Journal of Sensors and Actuators*, vol. 26, no. 9, pp. 1213–1218, 2013.

[7] H. Zhou, L. Hong, and Q. Cheng, "A low self-noise accelerometer based on piezoelectric bimorphs," *Journal of Chinese Inertial Technology*, vol. 28, no. 4, pp. 469–473, 2020.

[8] G. Xu, C. Wang, H. Yang, Y. Ma, and X. Chen, "Emulational analysis and design of anti-overload piezoelectric MEMS accelerometer for vibration monitoring of industrial equipment," *Instrument Technique and Sensor*, vol. 445, no. 2, pp. 28–32+55, 2020.

[9] Z. Qiu, J. Huang, and H. Hao, "Design and simulation on the suspension of MEMS sensor for low-frequency micro-seismic monitoring," *Mining Research and Development*, vol. 38, no. 11, pp. 113–118, 2018.

[10] A. T. Kollias and J. N. Avaritsiotis, "A study on the performance of bending mode piezoelectric accelerometers," *Sensors and Actuators A: Physical*, vol. 121, no. 2, pp. 434–442, 2005.

[11] D. Crescini, D. Marioli, E. Sardini, and A. Taroni, "Large bandwidth and thermal compensated piezoelectric thick-film acceleration transducer," *Sensors and Actuators A: Physical*, vol. 87, no. 3, pp. 131–138, 2001.

[12] L. P. Wang, R. A. Wolf, Y. Wang et al., "Design, fabrication, and measurement of high-sensitivity piezoelectric microelectromechanical systems accelerometers," *Journal of Microelectromechanical Systems*, vol. 12, no. 4, pp. 433–439, 2003.

[13] L. P. Wang, K. Deng, L. Zou, R. Wolf, R. J. Davis, and S. Trolier-McKinstry, "Microelectromechanical systems (MEMS) accelerometers using lead zirconate titanate thick films," *IEEE Electron Device Letters*, vol. 23, no. 4, pp. 182–184, 2002.

[14] K. Kim, S. Zhang, G. Salazar, and X. Jiang, "Design, fabrication and characterization of high temperature piezoelectric vibration sensor using YCOB crystals," *Sensors and Actuators A: Physical*, vol. 178, pp. 40–48, 2012.

[15] S. H. Choy, X. X. Wang, H. L. W. Chan, and C. L. Choy, "Study of compressive type accelerometer based on lead-free BNKBT piezoceramics," *Applied Physics A*, vol. 82, no. 4, pp. 715–718, 2006.

[16] P. A. Wlodkowski, D. Kan, and M. Kahn, "The development of high-sensitivity, low-noise accelerometers utilizing single crystal piezoelectric materials," *Sensors and Actuators A: Physical*, vol. 90, no. 1-2, pp. 125–131, 2001.

[17] C. Ai, X. Zhao, S. Li, Y. Li, Y. Bai, and D. Wen, "Fabrication and characteristic of a double piezoelectric layer acceleration sensor based on Li-doped ZnO thin film," *Micromachines (Basel)*, vol. 10, no. 5, p. 331, 2019.

[18] Q. Lu, J. Bai, K. Wang, and S. He, "Design, optimization, and realization of a high-performance MOEMS accelerometer from a double-device-layer SOI wafer," *Journal of Microelectromechanical Systems*, vol. 26, no. 4, pp. 859–869, 2017.

[19] W. R. Ali and M. Prasad, "Piezoelectric MEMS based acoustic sensors: a review," *Sensors and Actuators A: Physical*, vol. 301, p. 111756, 2020.

[20] S. Tadigadapa and K. Mateti, "Piezoelectric MEMS sensors: state-of-the-art and perspectives," *Measurement Science and Technology*, vol. 20, no. 9, p. 092001, 2009.

[21] T. Hou, H. Liu, J. Zhu et al., "Piezoelectric geophone: a review from principle to performance," *Ferroelectrics*, vol. 558, no. 1, pp. 27–35, 2020.

[22] Y. Xin, H. Sun, C. Guo et al., "Note: a novel cantilever beam for low-frequency high performance piezoelectric geophone," *The Review of Scientific Instruments*, vol. 88, no. 6, article 066105, 2017.

[23] M. K. Lee, S. H. Han, K. H. Park et al., "Design optimization of bulk piezoelectric acceleration sensor for enhanced performance," *Sensors (Basel)*, vol. 19, no. 15, p. 3360, 2019.

[24] S. Pyo, J. Kim, H. Kim, and Y. Roh, "Development of vector hydrophone using thickness-shear mode piezoelectric single crystal accelerometer," *Sensors and Actuators A: Physical*, vol. 283, pp. 220–227, 2018.

[25] J. C. Yu and C. B. Lan, "System modeling of microaccelerometer using piezoelectric thin films," *Sensors and Actuators A: Physical*, vol. 88, no. 2, pp. 178–186, 2001.

[26] A. Erturk and D. J. Inman, "Issues in mathematical modeling of piezoelectric energy harvesters," *Smart Materials and Structures*, vol. 17, no. 6, p. 065016, 2008.

[27] C. C. Hindrichsen, J. Larsen, E. V. Thomsen, K. Hansen, and R. Lou-Møller, "Circular piezoelectric accelerometer for high band width application," in *Proceedings of the 2009 IEEE Sensors*, pp. 475–478, Christchurch, New Zealand, 2009.

[28] C. Liu and Z. Fang, "Response surface method for complex mechanical assembly," *Journal of Xi'an Jiaotong University*, vol. 52, no. 9, pp. 28–36, 2018.

[29] X. Xu, Y. Li, G. Wang, X. Sun, and Y. Sun, "Design of six-axis force piezoelectric sensor with spoke structure," *Optics and Precision Engineering*, vol. 28, no. 12, pp. 2655–2664, 2020.

[30] B. Tian, H. Liu, N. Yang, Y. Zhao, and Z. Jiang, "Design of a piezoelectric accelerometer with high sensitivity and low transverse effect," *Sensors (Basel)*, vol. 16, no. 10, p. 1587, 2016.

[31] A. Sheikhaleh, K. Abedi, and K. Jafari, "A proposal for an optical MEMS accelerometer relied on wavelength modulation with one dimensional photonic crystal," *Journal of Lightwave Technology*, vol. 34, no. 22, pp. 5244–5249, 2016.

[32] D. Zhu, N. Wang, and M. Huang, "The analysis of the frequency response characteristics of the piezoelectricity acceleration geophone apllied to seismic exploration," *Journal of Railway Science and Engineering*, vol. 8, no. 5, pp. 113–118, 2011.

[33] Y. Yuan, D. Wang, X. Li et al., "Design of high sensitive piezoelectric accelerometer for nuclear power status monitoring," *Piezoelectrics & Acoustooptics*, vol. 41, no. 1, pp. 49–52, 2019.

[34] D. Huang, T. T. Allen, W. I. Notz, and N. Zeng, "Global optimization of stochastic black-box systems via sequential kriging meta-models," *Journal of Global Optimization*, vol. 34, no. 3, pp. 441–466, 2006.

[35] Z. Mohammed, W. A. Gill, and M. Rasras, "Modelling and optimization of inertial sensor-accelerometer," in *Outlook and Challenges of Nano Devices, Sensors, and MEMS*, pp. 331–345, Springer, 2017.

[36] H. Nozato, A. Oota, T. Ishigami, and T. Usuda, "The methods for the calibration of vibration pick-ups by laser interferometry: part V. Uncertainty evaluation on the ratio of transducer's peak output value to peak input acceleration in shock calibration," *Measurement Science and Technology*, vol. 22, no. 12, p. 125109, 2011.

[37] Y. Li, Y. Xu, J. Zhu et al., "Design, assembly and testing of a novel piezoelectric geophone based on PVDF film," *Integrated Ferroelectrics*, vol. 211, no. 1, pp. 69–81, 2020.